Nucleation of stoichiometric compounds from liquid: Role of the kinetic factor

H. Song,[1] Y. Sun,[1] F. Zhang,[1] C. Z. Wang,[1] K. M. Ho,[1,2,3] and M. I. Mendelev[1]

[1]*Division of Materials Sciences and Engineering, Ames Laboratory (US Department of Energy), Ames, Iowa 50011, USA*

[2]*Department of Physics, Iowa State University, Ames, Iowa 50011, USA*

[3]*Hefei National Laboratory for Physical Sciences at the Microscale and Department of Physics, University of Science and Technology of China, Hefei, Anhui 230026, China*

(Received 2 November 2017; published 20 February 2018)

The nucleation rate depends on the free-energy barrier and the kinetic factor. While the role of the free energy barrier is a text-book subject, the importance of the kinetic factor is frequently underestimated. In this study, we applied the mean first-passage time method, to obtain the free-energy landscape and kinetic factor directly from the molecular dynamics (MD) simulations of the nucleation of the face-centered cubic (fcc) phase in the pure Ni and the B2 phases in the $Ni_{50}Al_{50}$ and $Cu_{50}Zr_{50}$ alloys. The obtained data show that while the free-energy barrier for nucleation is higher in pure Ni the nucleation rate is considerably lower in the $Ni_{50}Al_{50}$ alloy. This result can be explained by the slow attachment kinetics in the $Ni_{50}Al_{50}$ alloy, which was related to the ordered nature of the B2 phase. Even smaller fraction of the antisite defects in the $Cu_{50}Zr_{50}$ alloy leads to such a slow attachment kinetics that the nucleation is never observed for this alloy in the course of the MD simulation. This is consistent with the experimental facts that the $Cu_{50}Zr_{50}$ alloy is a good glass forming alloy and the $Ni_{50}Al_{50}$ alloy is not. Thus the present study demonstrates that the atom attachment rate can be the critical factor that controls the nucleation process under certain conditions.

DOI: 10.1103/PhysRevMaterials.2.023401

I. INTRODUCTION

Crystal nucleation from the liquid has been extensively studied in the several past decades [1,2]. According to the classical nucleation theory (CNT) [3], forming a crystalline nucleus can be described as a competition between the bulk driving force and the energy penalty associated with creating an interface between the nucleus and liquid. The excess free energy to form a nucleus with n atoms can be expressed as $\Delta G = n\Delta\mu + A\gamma$, where $\Delta\mu$ (<0) is the difference between the bulk solid and liquid free energies, γ is the solid-liquid interfacial (SLI) free energy, and A is the interface area. When the crystal nucleus is small, its growth leads to increasing the free energy but once the nucleus is larger than the critical size n^*, its growth leads to decreasing the free energy. Thus, the excess of the free energy ΔG^* necessary to form the critical nucleus is considered as the nucleation barrier. Accordingly, the nucleation rate can be written as

$$J = \kappa \exp\left(-\frac{\Delta G^*}{k_B T}\right), \tag{1}$$

where

$$\kappa = \rho_L f^+_{n^*} Z \tag{2}$$

is the kinetic prefactor, which depends on the atomic density of the liquid phase ρ_L, the rate of attachment of atoms to the critical cluster $f^+_{n^*}$, and the Zeldovich factor Z [4], which describes the curvature of the free energy landscape at the top of the barrier $Z = \sqrt{|\Delta G''(n^*)|/2\pi k_B T}$.

It is the free energy barrier that is usually considered to dominate the nucleation rate J. Therefore it is frequently used to predict whether the nucleation will proceed fast or not. If we assume that the nucleus has a spherical shape, the nucleation energy barrier ΔG^* can be calculated as

$$\Delta G^{s*}_{\mathrm{CNT}} = \frac{16}{3}\pi \frac{\gamma^3}{\Delta\mu^2}. \tag{3}$$

Modern simulation techniques allow to obtain reliable data on the bulk driving forces, $\Delta\mu$ [5–7] and the SLI free energies at the melting temperatures, γ [8,9]. *However, how realistic are the predictions made based just on these data?* Consider as example the crystal nucleation in three systems described by the embedded atom method [10] (EAM) and the Finnis-Sinclair [11] potentials: pure Ni [12] [which has face-centered cubic (fcc) lattice] and B2 phases in the $Ni_{50}Al_{50}$ [13] and $Cu_{50}Zr_{50}$ [14] alloys. The bulk driving force and the SLI free energy were obtained for all of these systems from MD simulations [15,16] and $\Delta G^{s*}_{\mathrm{CNT}}$ is shown in Fig. 1. Examination of these data suggests that the nucleation will be the slowest in the pure Ni; it will proceed a little faster in the $Cu_{50}Zr_{50}$ alloy and very fast in the $Ni_{50}Al_{50}$ alloy. The MD simulation results are in vivid contradiction with this prediction: while no nucleation has been observed in the $Cu_{50}Zr_{50}$ alloy [17], it is readily observed in the pure Ni. We note that these MD simulation results are consistent with experimental observations: the $Cu_{50}Zr_{50}$ alloy is a good glass former [18], while no amorphous Ni sample has been synthesized. Moreover, the MD simulation shows that the nucleation in the pure Ni proceeds much faster than in the $Ni_{50}Al_{50}$ alloy (see below) while the data shown in Fig. 1 suggest the opposite. Thus, even if we use very accurate input data does not allow us to make realistic predictions based on Eq. (3).

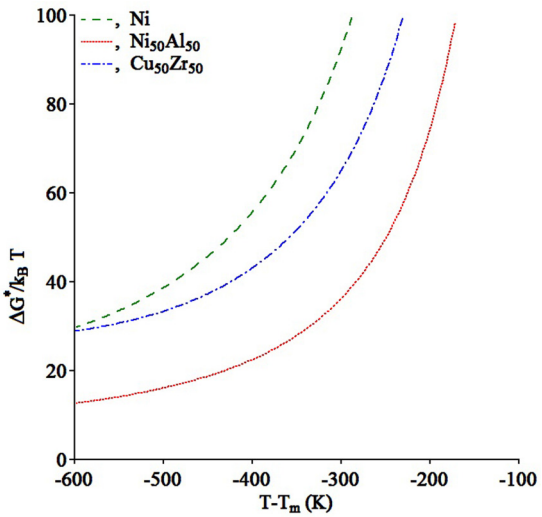

FIG. 1. Nucleation barriers according to Eq. (3) as a function of undercooling in the pure Ni and in the $Ni_{50}Al_{50}$ and $Cu_{50}Zr_{50}$ alloys.

Equation (3) is derived using several strong approximations: the nucleus is assumed to be spherical and the SLI free energy is assumed to be temperature and curvature independent. Recently, a considerable progress was achieved to evaluate activation barriers from simulation without making such approximations. For example, umbrella sampling [19,20] or transition path sampling [21] methods map out the equilibrium free energy landscape for nucleation by adding a biased potential to the interatomic interaction. However, these techniques do not provide any information about the nucleation kinetics. Auer and Frenkel proposed a method to obtain the attachment rate for the critical nucleus in Ref. [19]. Since the nucleation rate can be obtained directly from MD simulation (e.g., see Refs. [22,23]), this method in combination with the umbrella sampling or transition path sampling methods allows to evaluate the effect of the attachment kinetics on the nucleation rate. Even a more self-consistent approach can be employed based on the mean first-passage time (MFPT) method recently developed by Wedekind *et al.* [24–26]. This method is applicable to systems where nucleation can be observed in the unbiased MD simulation. The MFPT method yields the nucleation rate, the size of the critical embryo and the Zeldovich factor. Additionally, Wedekind *et al.* proposed to use the Fokker-Planck (FP) equation [27] to analyze the same MD simulation data and reconstruct the free energy landscape as well as the attachment rates as a function of embryo size [24,25]. Combination of this analysis with the nucleation rates obtained from the MFPT method can reveal how both the nucleation barrier and attachment rate affect the nucleation rate.

In this paper, we report the results of the systematic MD simulation study of the homogeneous nucleation in the pure Ni and $Ni_{50}Al_{50}$ and $Cu_{50}Zr_{50}$ alloys. The rest of the paper is organized as follows. In the next section, we will describe the application of the MFPT method to the systems under investigation. Then we will describe how we determined the nucleation barriers and the attachment rates. Finally, we will discuss the obtained results mostly focusing on the role of the attachment kinetics.

II. DETERMINATION OF NUCLEATION RATE

To describe the interatomic interactions in the pure Ni and $Ni_{50}Al_{50}$ and $Cu_{50}Zr_{50}$ alloys, we used the EAM/FS potentials developed in Refs. [12,13] and [14], respectively. The liquid models (32,000 atoms for the pure Ni and 54,000 atoms for the alloys) equilibrated at T_m during 2 ns were taken as the initial configurations (t_0), and the simulations were started by quenching the liquid to the chosen undercooling temperature ($\Delta T = 540$ K), which was approximately 30%–40% of T_m. The 200 independent simulations were performed for each system by setting the different initial velocity random at configuration t_0. To define crystal-like embryos, we employed the bond-orientational order parameter (BOO) [19,28,29], with the threshold chosen based on Espinosa *et al.*'s "equal mislabeling" method [30] for each simulation system. The crystal embryos were defined by the ten Wolde-Frenkel definition [19,29].

The MFPT method requires determination of the time when the *largest* crystal cluster in the system reaches or exceeds size n for the first time (first-passage time, τ). In the present study, we determined the number of atoms in the largest cluster every 50 fs. The simulation was terminated once the largest clusters exceeded 1000 atoms. It took from 100 ps to 150 ns to reach this state in the cases of the pure Ni and the $Ni_{50}Al_{50}$ alloy. However, for the $Cu_{50}Zr_{50}$ alloy, although small subclusters (i.e., crystal clusters with $n < n^*$) were detected, we never observed any nucleation during 200 ns. Thus the MFPT method could not be applied to this alloy. Examples of nucleation are shown in the insets of Fig. 2. In all simulation runs, we only observed one cluster passed the critical size at the moment. Typically, the pure Ni model contained more subclusters than did the $Ni_{50}Al_{50}$ alloy model. The critical nuclei in pure Ni were usually almost spherical while the critical nuclei in the $Ni_{50}Al_{50}$ alloy were very anisotropic. The time required to completely solidify the $Ni_{50}Al_{50}$ alloy model was much longer than that for the pure Ni.

The MFPT method relies on the Fokker-Planck equation [24,25], which relates the probability, P, to find a system at point n of the reaction coordinate at time t:

$$\frac{\partial P(n,t)}{\partial t} = \frac{\partial}{\partial n}\left[D(n)e^{-\Delta G(n)/k_BT}\frac{\partial}{\partial n}(P(n,t)e^{\Delta G(n)/k_BT})\right] = -\frac{\partial J(n,t)}{\partial n}, \quad (4)$$

where J(n,t) is the current, D(n) is a generalized diffusion coefficient, which in general depends on the state of the system, ΔG(n) is the free-energy landscape, T is the temperature, and k_B Boltzmann's constant. In the case of nucleation, the number of atoms in a nucleus can be used as n.

Wedekind *et al.* [25,31] defined the MFPT as the average time τ(n) that the system, starting out at n_0, needs to reach the state n for the first time; it can be presented as

$$\tau(n;n_0,a) = \int_{n_0}^{n}\frac{1}{D(y)}dy\, e^{\Delta G(y)/k_BT}\int_a^y dz e^{-\Delta G(z)/k_BT} \quad (5)$$

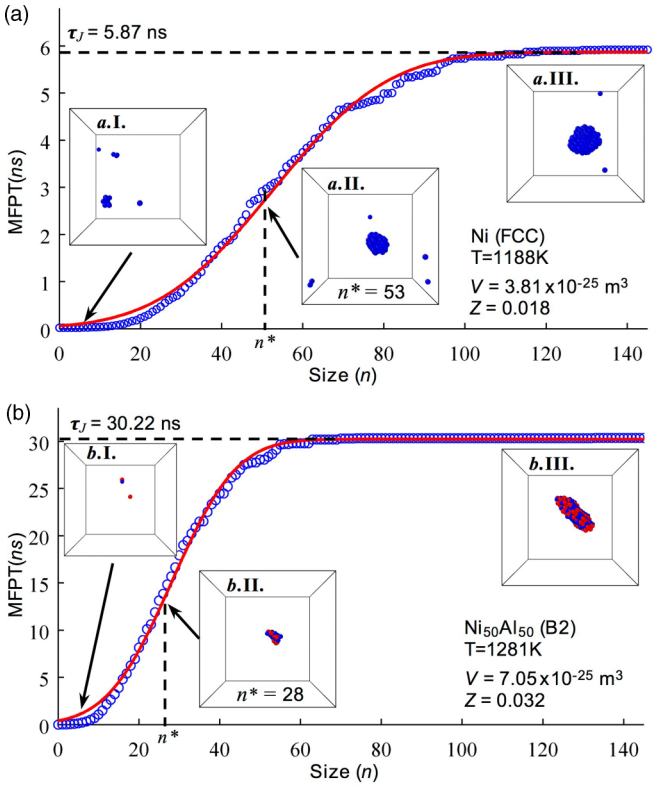

FIG. 2. Mean first-passage time $\tau(n)$ as a function of the cluster size n obtained from the MD simulations of (a) pure Ni and (b) $Ni_{50}Al_{50}$ alloys at the same undercooling $\Delta T = 540$ K. The solid lines (red) are fitted to Eq. (4). The insets show crystal clusters (I) before the nucleation, (II) when the clusters reached the corresponding critical sizes, and (III) when the clusters grow ten times of their critical sizes. Ni atoms are blue and Al atoms are red. Only the solidlike atoms determined by BOO are shown.

when the boundary conditions are reflecting at a, and absorbing at $n = b$ [25,32]. Therefore we recorded the time necessary for the *largest* cluster in the system to reach or exceed a given cluster size n for the first time (first-passage time) and averaged this time over 200 repetitions to obtain the *mean* first-passage time $\tau(n)$. Figure 2 shows the obtained functions $\tau(n)$. Due to sufficiently high nucleation barriers, these functions have a characteristic sigmoidal shape [25] with a clear plateau defined by the nucleation time τ_J. The MFPT can be expressed as a function of the largest cluster size as

$$\tau(n) = \frac{\tau_J}{2}[1 + erf(Z\sqrt{\pi}(n - n^*))]. \quad (6)$$

Fitting the simulation data shown in Fig. 2 to this equation allowed us to determine the nucleation time τ_J, the critical cluster size n^*, and the Zeldovich factor Z.

The nucleation rate can be obtained from the nucleation time τ_J as

$$J = \frac{1}{V\tau_J}, \quad (7)$$

where V is the system volume. The obtained values are presented in Fig. 2 and Table I. The examination of this table reveals that the critical nucleus size in the pure Ni is almost twice larger than that in the $Ni_{50}Al_{50}$ alloy, which is consistent with the prediction made based on Fig. 1. However, the nucleation rate in the pure Ni is ten times larger than that in the $Ni_{50}Al_{50}$ alloy.

TABLE I. Summary of calculated quantities for pure Ni and $Ni_{50}Al_{50}$ ($\Delta T = 540$ K).

Quantity	Ni	$Ni_{50}Al_{50}$
N	32 000	54 000
T	1188 K	1281 K
ρ	8.40×10^{28} m^{-3}	7.66×10^{28} m^{-3}
n^*_{MFPT}	53 ± 1	28 ± 1
n^*	55	24
$\Delta G^*/k_BT$	19.6 ± 0.1	17.9 ± 0.1
$\Delta G^*_{\mathrm{CNT}}/k_BT$	12.73	9.20
$f^+_{n^*}$	$(1.07 \pm 0.6) \times 10^{14}$ s^{-1}	$(1.26 \pm 0.6) \times 10^{12}$ s^{-1}
f^*_D	$(9.56 \pm 0.1) \times 10^{13}$ s^{-1}	$(3.7 \pm 0.2) \times 10^{12}$ s^{-1}
Z	0.0178 ± 0.0004	0.032 ± 0.001
J	4.97×10^{32}(m^3 s)$^{-1}$	4.71×10^{31}(m^3 s)$^{-1}$
J_{MFPT}	$(4.47 \pm 0.02) \times 10^{32}$(m^3 s)$^{-1}$	$(4.69 \pm 0.02) \times 10^{31}$(m^3 s)$^{-1}$
J_{CNT}	5.36×10^{35}(m^3 s)$^{-1}$	1.45×10^{36}(m^3 s)$^{-1}$

III. DETERMINATION OF NUCLEATION BARRIER AND ATTACHMENT RATE

To explain this result, we need to separate the contributions of the nucleation barrier and the atom attachment kinetics to the nucleation rate. To determine the free-energy barrier for the nucleation, we used the method developed by Wedekind and Reguera [24,26]. This method required only two ingredients: the steady-state probability distribution and the MFPT to reconstruct the free-energy landscape. Both ingredients can be directly obtained from the MD simulation. In particular, Wedekind *et al.* choose the largest embryo in the system as the appropriate order parameter to track the MFPT $\tau(n)$ and steady-state probability distribution $P^{\mathrm{st}}_{\mathrm{larg}}(n)$. Following Refs. [24,26], we first calculated

$$B(n) = -\frac{1}{P^{\mathrm{st}}_{\mathrm{larg}}(n)}\left[\int_n^b P^{\mathrm{st}}_{\mathrm{larg}}(n')dn' - \frac{\tau(b) - \tau(n)}{\tau(b)}\right], \quad (8)$$

where b is an upper boundary that we sample both for $\tau(n)$ and $P^{\mathrm{st}}_{\mathrm{larg}}(n)$, which means that once the largest embryo has passed through this boundary in a simulation, the following time steps are discarded from the statistics. We chose $b = 140$ for the pure Ni, and $b = 70$ for $Ni_{50}Al_{50}$. Both of the b boundaries are more than twice of the critical nucleus sizes in each system. Then, the free energy $\Delta G_{\mathrm{larg}}(n)$ is reconstructed by

$$\frac{\Delta G_{\mathrm{larg}}(n)}{k_BT} = \ln\left(\frac{B(n)}{B(n_1)}\right) - \int_{n_1}^{n}\frac{dn'}{B(n')} + C, \quad (9)$$

for any desired interval $[n_1 \leqslant n \leqslant b]$. As a reference point we used $n_1 = 1$, and the constant C is applied to match up curve $\Delta G_{\mathrm{larg}}(n)/k_BT$ with $-\ln(P^{\mathrm{st}}_{\mathrm{larg}}(n))$ in certain n range (see below).

The equilibrium distribution of embryos can be described by [2,33]

$$P^{\mathrm{st}}(n) = \frac{N_n}{N} = \exp\left[-\frac{\Delta G(n)}{k_BT}\right], \quad (10)$$

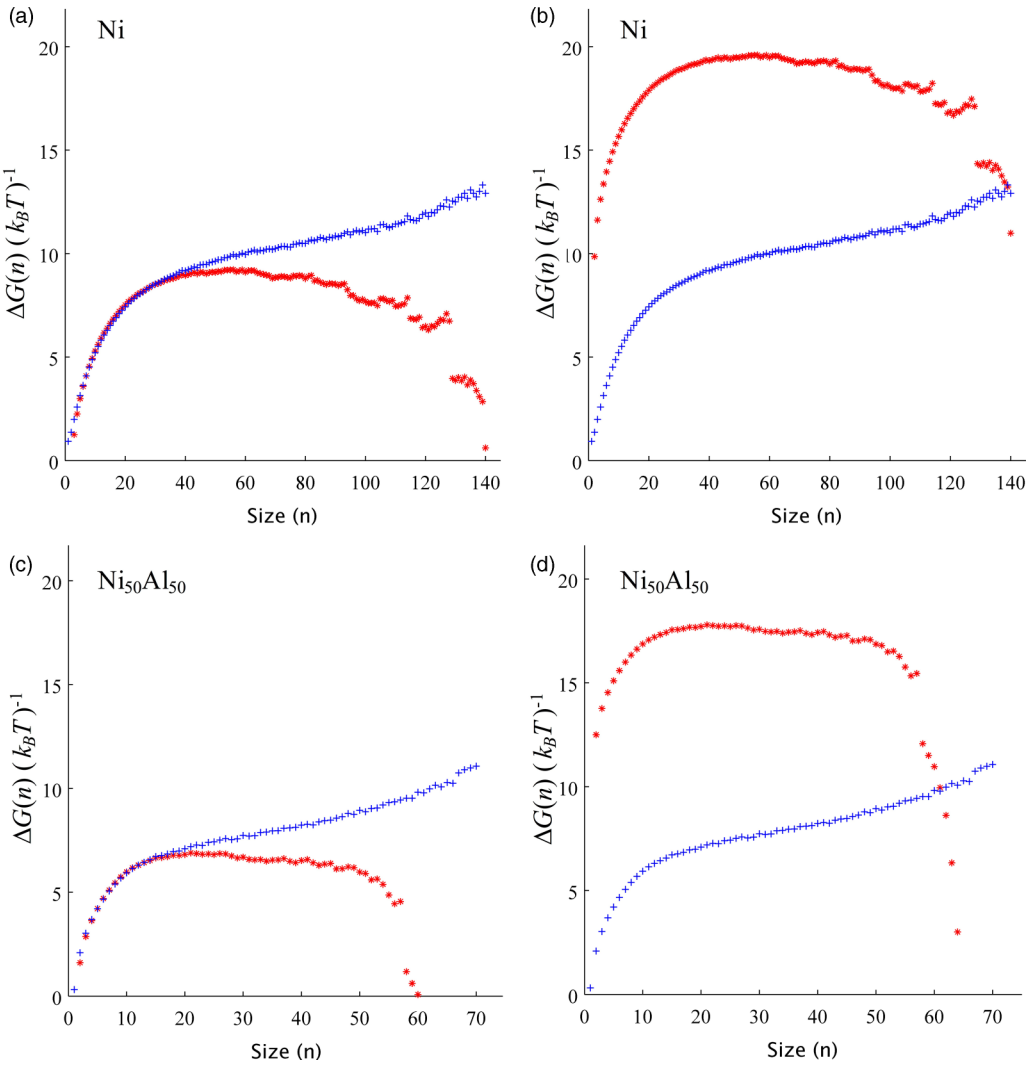

FIG. 3. Free-energy landscape for the nucleation in [(a) and (b)] the pure Ni and [(c) and (d)] $Ni_{50}Al_{50}$ alloy. Red stars represent $\Delta G_{\mathrm{larg}}(n)/k_BT$, and blue crosses represent $-\ln(P^{\mathrm{st}}_{\mathrm{larg}}(n))$. In (a) and (c), $\Delta G_{\mathrm{larg}}(n)/k_BT$ curves are lined up with $-\ln(P^{\mathrm{st}}_{\mathrm{larg}}(n))$ in the region before the critical sizes by the constant C in Eq. (9). Plots in (b) and (d) show the true free-energy landscapes by shifting the $\Delta G_{\mathrm{larg}}/k_BT$ curves by ln(N) in each system.

where N_n is the number of embryos of size n in a system containing N atoms. The steady-state probability distribution $P^{\mathrm{st}}(n)$ for any embryo size n can be approximated by $P^{\mathrm{st}}(n) = N_n/N$. However, the probability distribution of the largest embryo $P^{\mathrm{st}}_{\mathrm{larg}}(n)$ is *unequal* to the full probability distribution of all the embryos $P^{\mathrm{st}}(n)$ in the system [34]. Instead, $P^{\mathrm{st}}_{\mathrm{larg}}(n)$ should be considered as the probability of forming exactly *one* (the largest) embryo in the system. Thus both $P^{\mathrm{st}}_{\mathrm{larg}}(n)$ and $P^{\mathrm{st}}(n)$ are related in a similar fashion by $\frac{P^{\mathrm{st}}_{\mathrm{larg}}(n)}{N} \approx P^{\mathrm{st}}(n)$, and the free energies for the largest or any cluster are connected by the simple relation $\Delta G(n) = \Delta G_{\mathrm{larg}}(n) + k_BT\ln(N)$ [26]. Lundrigan and Saika-Voivod indicated that in a high free-energy barrier nucleation, larger embryos are rare, when a large embryo is present, there is approximately no other embryo of that size or larger in the system [35]. Therefore, for large embryo size, $\frac{P^{\mathrm{st}}_{\mathrm{larg}}(n)}{N}$ and $P^{\mathrm{st}}(n)$ are approximately equal to each other. The curves $\Delta G_{\mathrm{larg}}(n)/k_BT$ and $-\ln(P^{\mathrm{st}}_{\mathrm{larg}}(n))$ are shown in Figs. 3(a) and 3(c) for the pure Ni and $Ni_{50}Al_{50}$ alloy, respectively. According to Eq. (10), $-\ln(P^{\mathrm{st}}_{\mathrm{larg}}(n))$ can be a reference for the nucleation free energy for small cluster sizes, since the small clusters are nearly equilibrium. However, upon approaching the critical size and beyond it, the continuously upward $-\ln(P^{st}_{\mathrm{larg}}(n))$ curve shows that the free energy landscape cannot be recovered by simply using Eq. (10) since the formation of a cluster in MD is not an equilibrium process and the probability distribution we collected from the simulation is not the equilibrium one. Consequently, we used only the $-\ln(P^{\mathrm{st}}_{\mathrm{larg}}(n))$ curve at small n as the reference to line up the $\Delta G_{\mathrm{larg}}(n)/k_BT$ curve by the constant C in Eq. (9). Figures 3(a) and 3(c) show an excellent agreement between the $\Delta G_{\mathrm{larg}}(n)/k_BT$ and $-\ln(P^{\mathrm{st}}_{\mathrm{larg}}(n))$ curves at small n after aligning by C. Now the true free-energy landscapes $\Delta G(n)/k_BT$ can be obtained by shifting the $\Delta G_{\mathrm{larg}}(n)/k_BT$ curves by $\ln(N)$, which is shown in Figs. 3(b) and 3(d). Lundrigan and Saika-Voivod used the Monte Carlo (MC) simulation with the umbrella sampling method [35] to verify the free-energy landscapes obtained by the MFPT method.

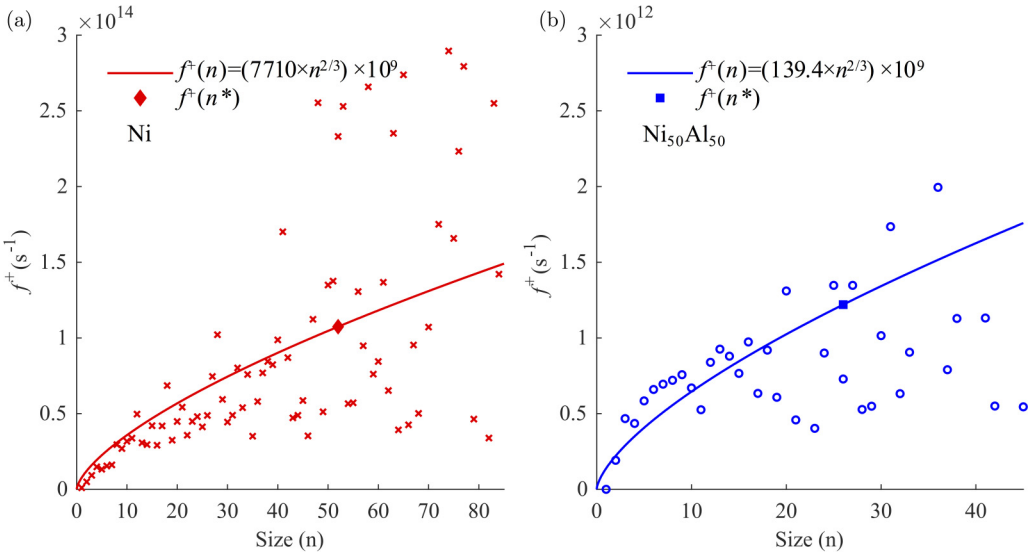

FIG. 4. The atom attachment rates as a function of the cluster size n in (a) the pure Ni and (b) $Ni_{50}Al_{50}$ alloy. The solid lines are the fittings to $f^+(n) = D_0 n^{2/3}$, and the solid points show the attachment rates $f^+(n^*)$ at the critical nucleus size n^*.

They pointed out that although there is a minor deviation in the small cluster size range, both methods show a very good agreement at the nucleation energy barrier.

The atom attachment rates as a function of n can be obtained from the MFPT and $P^{st}_{larg}(n)$ data [24,35] as

$$f^+(n) = \frac{B(n)}{\left(\frac{\partial \tau(n)}{\partial n}\right)}. \tag{11}$$

We assume that the rate of attachment of an atom to the critical cluster is the same for any of the largest clusters. We also applied the method developed by Auer and Frenkel [19] to calculate the single point for f_D^* at the critical nucleus size n^*. Figures 4(a) and 4(b) (also see Table I) show that although there is some noise from $P^{st}_{larg}(n)$ at the large cluster size, the agreement near n^* between the two methods is acceptable.

Figure 5(a) compares the reconstructed true free energy curve $\Delta G(n)/k_BT$ as a function of size n for both Ni and $Ni_{50}Al_{50}$. This analysis leads to $\Delta G^*/k_BT = 19.5$ and $n^* = 53$ for the pure Ni, and $\Delta G^*/k_BT = 17.9$ and $n^* = 28$ for $Ni_{50}Al_{50}$. The obtained values of the critical nucleus size are different by $2 \sim 4$ atoms comparing to the corresponding MFPT values described above. This corresponds to $\sim 0.02\, k_BT$ difference in the free energy, which is much smaller than the calculation error, $\pm 0.1\, k_BT$. Figure 5(b) shows the attachment rate as a function of size n, with the solid line fit to $f^+(n) = D_0 n^{2/3}$ [35].

IV. DISCUSSION

Table I gives a summary of all quantities for characterizing the nucleation process. Using the values of $\Delta G^*/k_BT$, ρ_L, Z,

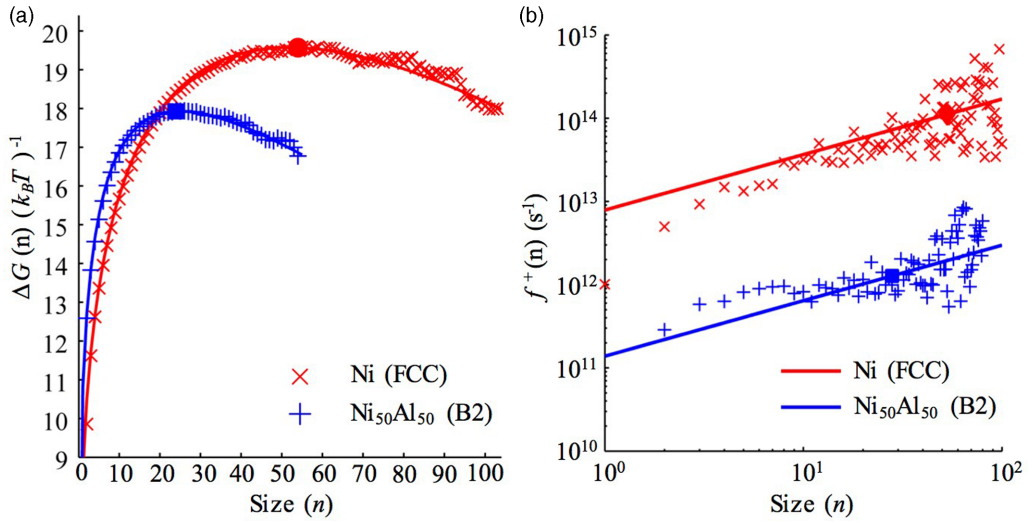

FIG. 5. (a) The true free energy curve $\Delta G(n)/k_BT$ calculated by the Wedeking and Reguera's method and shifted according to the system size N. The solid points show the critical nucleation barriers. The solid lines are the fitting to $-an + bn^{2/3} + cn^{1/3}$. (b) The attachment rate as a function of size n. The solid lines are the fitting to $f^+(n) = D_0 n^{2/3}$, and the solid points are the attachment rates at the critical size $f^+_{n^*}$.

and $f_{n^*}^+$, we can calculate the nucleation rate J according to Eqs. (1) and (2), and they are very close to the values obtained directly by fitting to the MFPT curves (J_{MFPT}). To evaluate the accuracy of our data and the CNT predictions, we performed the following calculations. First, the attachment rate can be also evaluated by measuring the effective attachment rate at the critical nucleus size [19,35]. The obtained attachment rates f_D^* are close to the values obtained from the MFPT method (see Table I). Second, using n^* obtained from the MFPT method, the free-energy barrier within the CNT can be calculated according to the spherical nucleus shape assumption [36]. The CNT predicts a lower barrier ($\Delta G_{\mathrm{CNT}}^*$ in Table I) for both systems but still $\Delta G_{\mathrm{CNT}}^{*\mathrm{Ni}} > \Delta G_{\mathrm{CNT}}^{*\mathrm{Ni_{50}Al_{50}}}$. However, the CNT suggests much higher nucleation rates for both cases and most importantly $J_{\mathrm{CNT}}^{\mathrm{Ni}} < J_{\mathrm{CNT}}^{\mathrm{Ni_{50}Al_{50}}}$, which contradicts our MD simulation observation. Furthermore, the $\Delta G(n)$ profiles showed in Fig. 5(a) are not well fitting to the traditional CNT described, i.e., $(-an + bn^{2/3})$, but could be significantly improved by adding a curvature correction term ($n^{1/3}$). Similar results also reported in other nucleation studies [35,37,38], and our results indicate that the nucleus shape may seriously affect the energy barrier especially when the critical nucleus size is pretty small.

The MD simulation shows how pronounced the effect of the attachment kinetics can be: the nucleation barrier is higher in the pure Ni than that in the $Ni_{50}Al_{50}$ alloy and yet the nucleation rate is ten times higher in the pure Ni. This effect of the attachment kinetics is even more pronounced in the $Cu_{50}Zr_{50}$ alloy. Based on the data presented in Fig. 1, the nucleation barrier in the $Cu_{50}Zr_{50}$ alloy should be between those in the pure Ni and the $Ni_{50}Al_{50}$ alloy. These estimations are made based on the CNT and as we showed above can be considerably different from the actual values. However, if we assume that the CNT at least reproduces the correct trend, we should observe comparable nucleation rates in these alloys. In reality, no nucleation was observed in the $Cu_{50}Zr_{50}$ alloy even at higher undercoolings ($\Delta T > 600$ K). Therefore the atom attachment kinetics in the $Cu_{50}Zr_{50}$ alloy should be much slower than that in the $Ni_{50}Al_{50}$ alloy. To verify this point, we need to compare the atom attachment rate at the critical size in both alloys. Unfortunately, since the B2 phase never nucleates in the $Cu_{50}Zr_{50}$ alloy in the MD simulation, we cannot directly evaluate the nucleation quantities in this alloy using the methods described above. Therefore we employed the isoconfigurational method proposed in Ref. [39] to get a rough estimation of the critical nucleus size and the effective attachment rate f_D^* at this size. In order to do it, we inserted seeds of the B2 phase of different sizes in the $Cu_{50}Zr_{50}$ liquid model containing ~16,000 atoms at $T = 786$ K ($\Delta T = 540$ K) and performed 30 independent MD runs for each seed. The B2 phases seed with a size of 32 atoms showed a 50/50 chance to melt or grow and, hence, was considered it as the critical size nucleus. The effective attachment rate [19,35] at this size was found to be $f_D^* = 4.52 \times 10^{10}\ \mathrm{s}^{-1}$. Thus the ratio of the critical sizes obtained from the MD simulation ($n_{\mathrm{Ni}}^* > n_{\mathrm{Cu_{50}Zr_{50}}}^* > n_{\mathrm{Ni_{50}Al_{50}}}^*$) does coincide with the trend predicted by the CNT and it is the extremely low attachment rate in the $Cu_{50}Zr_{50}$ alloy (which is around two orders of magnitude lower than that in the $Ni_{50}Al_{50}$ alloy) that makes the nucleation so slow.

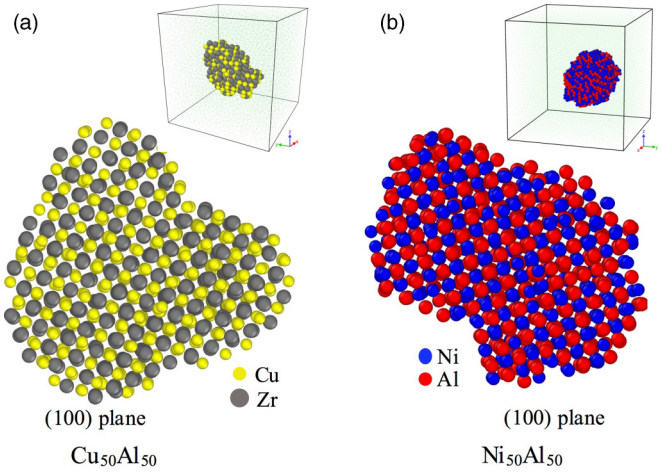

FIG. 6. The cross-section views of the (100) planes of growing B2 phases in (a) the $Cu_{50}Zr_{50}$ and (b) $Ni_{50}Al_{50}$ alloys.

The difference in the attachment rates in the studied systems can be only partially explained by the difference in the liquid atomic diffusivities in these alloys. The diffusion coefficients obtained from the mean square displacements at the same undercoolings are $D_{\mathrm{Ni}} = 8.8 \times 10^{-6}\ \mathrm{cm}^2/\mathrm{s}$ in the pure Ni, $D_{\mathrm{Ni}} = 8.6 \times 10^{-6}\ \mathrm{cm}^2/\mathrm{s}$ and $D_{\mathrm{Al}} = 7.2 \times 10^{-6}\ \mathrm{cm}^2/\mathrm{s}$ in the $Ni_{50}Al_{50}$ alloy, $D_{\mathrm{Cu}} = 3.5 \times 10^{-7}\ \mathrm{cm}^2/\mathrm{s}$ and $D_{\mathrm{Zr}} = 2.0 \times 10^{-7}\ \mathrm{cm}^2/\mathrm{s}$ in the $Cu_{50}Zr_{50}$ alloy. Based on these data, the attachment rate in the pure Ni should be about the same as in the $Ni_{50}Al_{50}$ alloy, which is not the case as we discussed above. In the $Cu_{50}Zr_{50}$ alloy, Zr diffuses 36 times slower than does Al in the $Ni_{50}Al_{50}$ alloy. However, the difference in the attachment rates is 82 times. The additional contribution in the slower attachment kinetics in the studied alloys is probably associated with the ordered character of the B2 phase: much less fraction of the atomic jumps from the liquid phase to the growing crystal will be successful because an atom should jump into the "right" site. Of course, from time to time, an atom can jump into a "wrong" site and form an antisite defect and MD simulation shows that the $Ni_{50}Al_{50}$ B2 phase grows from the liquid phase with a considerable amount of such defects [40]. We can speculate that the less growing crystal phase is tolerant to such defects the faster the attachment kinetics should be. To test this assumption, we compared the density of antisite defect in the $Ni_{50}Al_{50}$ and $Cu_{50}Zr_{50}$ alloys obtained by the seeding method. In both cases the seeds were larger than the critical nuclei such that the B2 phase grew from the liquid, and only the data from the as grown B2 phase were considered. Examples of the cross-section views are shown in Fig. 6. Vividly, the growing B2 phase in the $Cu_{50}Zr_{50}$ alloy is more ordered than that in the $Ni_{50}Al_{50}$ alloy. Indeed, it was found that the new forming B2 phase in the $Ni_{50}Al_{50}$ alloy contains 15.2% antisite defects, while their concentration in the $Cu_{50}Zr_{50}$ alloy is only 9.1%. The antisite defect concentration in the B2 phase, which spontaneously nucleated in the $Ni_{50}Al_{50}$ alloy, was found to be 15.8%. The similarity of the antisite defect concentrations obtained from the nucleation and seeded simulation shows that the atomic ordering does not come from the artificial seeds, but from the physical nature of the stoichiometric compound.

A rigorous analysis of the tolerance to the antisite defects requires the knowledge of the antisite defect formation free energy. Determination of this quantity is a subject of a separate study. In the present study, we simply determined the antisite formation energy and found that this quantity is equal to 1.6 eV in the Ni-Al B2 phase and 2.0 eV in the Cu-Zr B2 phase. Therefore the $Cu_{50}Zr_{50}$ B2 phase is indeed less tolerant to the antisite defects than the $Ni_{50}Al_{50}$ B2 phase. The stronger atomic ordering results in the lower atom attachment rate, and hence, a low nucleation rate in the $Cu_{50}Zr_{50}$ alloy.

It should be noted that a high antisite defect concentration has been observed in the growing Ni-Al B2 phase in the simulation of the nominally flat SLI migration [41], where it was "interpreted to arise from disorder trapping during the rapid solidification." This interpretation cannot be applied to the nucleation considered in the present study because the driving force and the average SLI velocity in the case of critical nucleus is zero.

Finally, it should be noted that, as in Ref. [42], the heat generation during the MD simulation of solidification can lead to considerable underestimation of the SLI velocity. The larger the SLI velocity, the larger the effect. Although, the attachment rate for Ni may be underestimated because of this effect, the underestimation will be much smaller in the case of the Ni-Al B2 phase, and it will be completely negligible in the case of the Cu-Zr B2 phase. Therefore this effect will not change our conclusion about the importance of the attachment kinetics, because it leads to larger underestimations in both the nucleation rate and the attachment kinetics for pure Ni than for the Ni-Al B2 phase. Moreover, with the account of this effect, the importance of the attachment rate will be even larger.

V. CONCLUSIONS

In summary, we employed MD simulations to study the crystal nucleation from the liquid in the pure Ni, $Ni_{50}Al_{50}$, and $Cu_{50}Zr_{50}$ alloys. Only the first two systems exhibited nucleation in the course of the MD simulation. Application of the MFPT method revealed that in spite of the fact that the nucleation barrier is higher in the pure Ni the nucleation rate is also higher in the pure Ni. This was attributed to the slow atom attachment kinetics in the $Ni_{50}Al_{50}$ alloy, which was related to the ordered nature of the B2 phase. The even lower fraction of the antisite defects in the $Cu_{50}Zr_{50}$ alloy explains why the nucleation is never observed for this alloy in the course of the MD simulation. This is consistent with the experimental facts that $Cu_{50}Zr_{50}$ alloy is a good glass forming alloy and the $Ni_{50}Al_{50}$ alloy is not. The current paper demonstrates that the atom attachment rate can be the critical factor to limit the nucleation process under certain conditions and suggests a new direction in the future nucleation studies in the alloys with stoichiometric compounds focusing on their tolerance to the antisite defects.

ACKNOWLEDGMENTS

We thank M. J. Kramer, R. E. Napolitano, X. Song, and R. T. Ott from Ames Laboratory for valuable discussion. This work was supported by the US Department of Energy (DOE), Office of Science, Basic Energy Sciences, Materials Science, and Engineering Division. The research was performed at Ames Laboratory, which is operated for the US DOE by Iowa State University under Contract No. DEAC02-07CH11358.

[1] K. F. Kelton and A. L. Greer, *Nucleation in Condensed Matter Applications in Materials and Biology*, 1st ed. (Elsevier, Amsterdam, 2010).

[2] P. G. Debenedetti, *Metastable Liquids: Concepts and Principles* (Princeton University Press, Princeton, New Jersey, 1996).

[3] D. Kashchiev, *Nucleation: Basic Theory with Applications* (Butterworth-Heinemann, London, 2000).

[4] J. B. Zeldovich, Acta Physicochim, URSS **18**, 1 (1943).

[5] P. Saidi, T. Frolov, J. J. Hoyt, and M. Asta, An angular embedded atom method interatomic potential for the aluminum–silicon system, Modell. Simul. Mater. Sci. Eng. **22**, 055010 (2014).

[6] H. Song and J. J. Hoyt, A molecular dynamics simulation study of the velocities, mobility and activation energy of an austenite-ferrite interface in pure Fe, Acta Mater. **60**, 4328 (2012).

[7] D. Y. Sun, M. I. Mendelev, C. A. Becker, K. Kudin, T. Haxhimali, M. Asta, J. J. Hoyt, A. Karma, and D. J. Srolovitz, Crystal-melt interfacial free energies in hcp metals: A molecular dynamics study of Mg, Phys. Rev. B **73**, 024116 (2006).

[8] J. J. Hoyt, M. Asta, and A. Karma, Method for Computing the Anisotropy of the Solid-Liquid Interfacial Free Energy, Phys. Rev. Lett. **86**, 5530 (2001).

[9] R. L. Davidchack and B. B. Laird, Direct Calculation of the Hard-Sphere Crystal/Melt Interfacial Free Energy, Phys. Rev. Lett. **85**, 4751 (2000).

[10] M. S. Daw and M. I. Baskes, Embedded-atom method - derivation and application to impurities, surfaces, and other defects in metals, Phys. Rev. B **29**, 6443 (1984).

[11] M. W. Finnis and J. E. Sinclair, A simple empirical n-body potential for transition-metals, Philos. Mag. A **50**, 45 (1984).

[12] M. I. Mendelev, M. J. Kramer, S. G. Hao, K. M. Ho, and C. Z. Wang, Development of interatomic potentials appropriate for simulation of liquid and glass properties of $NiZr_2$ Alloy, Philos. Mag. **92**, 4454 (2012).

[13] G. P. P. Pun and Y. Mishin, Development of an interatomic potential for the Ni-Al system, Philos. Mag. **89**, 3245 (2009).

[14] M. I. Mendelev, M. J. Kramer, R. T. Ott, D. J. Sordelet, D. Yagodin, and P. Popel, Development of suitable interatomic potentials for simulation of liquid and amorphous Cu–Zr alloys, Philos. Mag. **89**, 967 (2009).

[15] S. R. Wilson and M. I. Mendelev, Dependence of solid-liquid interface free energy on liquid structure, Modell. Simul. Mater. Sci. Eng. **22**, 065004 (2014).

[16] S. R. Wilson, K. G. S. H. Gunawardana, and M. I. Mendelev, Solid-liquid interface free energies of pure bcc metals and B2 phases, J. Chem. Phys. **142**, 134705 (2015).

[17] C. G. Tang and P. Harrowell, Anomalously slow crystal growth of the glass-forming alloy CuZr, Nat. Mater. **12**, 507 (2013).

[18] M. I. Mendelev, M. J. Kramer, R. T. Ott, D. J. Sordelet, M. F. Besser, A. Kreyssig, A. I. Goldman, V. Wessels, K. K. Sahu, K. F.

Kelton, R. W. Hyers, S. Canepari, and J. R. Rogers, Experimental and computer simulation determination of the structural changes occurring through the liquid-glass transition in Cu-Zr alloys, Philos. Mag. **90**, 3795 (2010).

[19] S. Auer and D. Frenkel, Numerical prediction of absolute crystallization rates in hard-sphere colloids, J. Chem. Phys. **120**, 3015 (2004).

[20] S. Auer and D. Frenkel, Suppression of crystal nucleation in polydisperse colloids due to increase of the surface free energy, Nature (London) **413**, 711 (2001).

[21] P. G. Bolhuis, D. Chandler, C. Dellago, and P. L. Geissler, Transition path sampling: Throwing ropes over rough mountain passes, in the dark, Annu. Rev. Phys. Chem. **53**, 291 (2002).

[22] R. S. Aga, J. R. Morris, J. J. Hoyt, and M. Mendelev, Quantitative Parameter-Free Prediction of Simulated Crystal-Nucleation Times, Phys. Rev. Lett. **96**, 245701 (2006).

[23] G. Chkonia, J. Wölk, R. Strey, J. Wedekind, and D. Reguera, Evaluating nucleation rates in direct simulations, J. Chem. Phys. **130**, 064505 (2009).

[24] J. Wedekind and D. Reguera, Kinetic reconstruction of the free-energy landscape, J. Phys. Chem. B **112**, 11060 (2008).

[25] J. Wedekind, R. Strey, and D. Reguera, New method to analyze simulations of activated processes, J. Chem. Phys. **126**, 134103 (2007).

[26] J. Wedekind, G. Chkonia, J. Wolk, R. Strey, and D. Reguera, Crossover from nucleation to spinodal decomposition in a condensing vapor, J. Chem. Phys. **131**, 114506 (2009).

[27] D. Reguera, J. M. Rubi, and J. M. G. Vilar, The mesoscopic dynamics of thermodynamic systems, J. Phys. Chem. B **109**, 21502 (2005).

[28] P. R. ten Wolde, M. J. Ruiz-Montero, and D. Frenkel, Numerical Evidence for BCC Ordering at the Surface of a Critical Fcc Nucleus, Phys. Rev. Lett. **75**, 2714 (1995).

[29] P. R. ten Wolde, M. J. Ruiz-Montero, and D. Frenkel, Numerical calculation of the rate of crystal nucleation in a Lennard-Jones system at moderate undercooling, J. Chem. Phys. **104**, 9932 (1996).

[30] J. R. Espinosa, C. Vega, C. Valeriani, and E. Sanz, Seeding approach to crystal nucleation, J. Chem. Phys. **144**, 034501 (2016).

[31] J. Wedekind, J. Wolk, D. Reguera, and R. Strey, Nucleation rate isotherms of argon from molecular dynamics simulations, J. Chem. Phys. **127**, 154515 (2007).

[32] P. Hanggi, P. Talkner, and M. Borkovec, Reaction-rate theory: Fifty years after Kramers, Rev. Mod. Phys. **62**, 251 (1990).

[33] S. Auer and D. Frenkel, Quantitative prediction of crystal-nucleation rates for spherical colloids: A computational approach, Annu. Rev. Phys. Chem. **55**, 333 (2004).

[34] S. Chakrabarty, M. Santra, and B. Bagchi, A Reply to the Comment on "Elucidating the Mechanism of Nucleation near the Gas-Liquid Spinodal", Phys. Rev. Lett. **101**, 019602 (2008).

[35] S. E. M. Lundrigan and I. Saika-Voivod, Test of classical nucleation theory and mean first-passage time formalism on crystallization in the Lennard-Jones liquid, J. Chem. Phys. **131**, 104503 (2009).

[36] Y. Sun, H. Song, F. Zhang, L. Yang, Z. Ye, M. I. Mendelev, C. Wang, and K. Ho, Overcoming the Time Limitation in Molecular Dynamics Simulation of Crystal Nucleation: A Persistent-Embryo Approach [Phys. Rev. Lett. (to be published)].

[37] S. Prestipino, A. Laio, and E. Tosatti, Shape and area fluctuation effects on nucleation theory, J. Chem. Phys. **140**, 094501 (2014).

[38] S. Prestipino, A. Laio, and E. Tosatti, Systematic Improvement of Classical Nucleation Theory, Phys. Rev. Lett. **108**, 225701 (2012).

[39] A. Widmer-Cooper, P. Harrowell, and H. Fynewever, How Reproducible are Dynamic Heterogeneities in a Supercooled Liquid? Phys. Rev. Lett. **93**, 135701 (2004).

[40] A. Kerrache, J. Horbach, and K. Binder, Molecular-dynamics computer simulation of crystal growth and melting in $Al_{50}Ni_{50}$, Epl **81**, 58001 (2008).

[41] X. Q. Zheng, Y. Yang, Y. F. Gao, J. J. Hoyt, M. Asta, and D. Y. Sun, Disorder trapping during crystallization of the B2-ordered NiAl compound, Phys. Rev. E **85**, 041601 (2012).

[42] J. Monk, Y. Yang, M. I. Mendelev, M. Asta, J. J. Hoyt, and D. Y. Sun, Determination of the crystal-melt interface kinetic coefficient from molecular dynamics simulations, Modell. Simul. Mater. Sci. Eng. **18**, 015004 (2010).